Journal of Manufacturing Processes 54 (2020) 228–239

Contents lists available at ScienceDirect

Journal of Manufacturing Processes

journal homepage: www.elsevier.com/locate/manpro

Filler metal distribution and processing stability in laser-arc hybrid welding of thick HSLA steel

Ivan Bunaziv[a,*], Sigurd Wenner[a], Xiaobo Ren[a], Jan Frostevarg[b], Alexander F.H. Kaplan[b], Odd M. Akselsen[a]

[a] SINTEF Industry, P.O. Box 4760 Torgarden, NO-7465 Trondheim, Norway
[b] Luleå University of Technology, Department of Engineering Sciences and Mathematics, SE-97187 Luleå, Sweden

ARTICLE INFO

Keywords:
Laser-arc hybrid welding
High strength steel
Thick steel
Non-metallic inclusions
Filler metal distribution
Microstructure
Mechanical properties

ABSTRACT

Welds made by high power laser beam have deep and narrow geometry. Addition of filler wire by the arc source, forming the laser-arc hybrid welding (LAHW) process, is very important to obtain required mechanical properties. Distribution of molten wire throughout the entire weld depth is of concern since it tends to have low transportation ability to the root. Accurate identification of filler metal distribution is very challenging. Metal-cored wires can provide high density of non-metallic inclusions (NMIs) which are important for acicular ferrite nucleation. Accurate filler distribution can be recognized based on statistical characterization of NMIs in the weld. In the present study, it was found that the amount of filler metal decreased linearly towards the root. The filler metal tends to accumulate in the upper part of the weld and has a steep decrease at 45–55 % depth which also has wavy pattern based on longitudinal cuts. Substantial hardness variation in longitudinal direction was observed, where in the root values can reach > 300 HV. Excessive porosity was generated at 75 % depth due to unstable and turbulent melt flow based on morphology of prior austenite grains. The delicate balance of process parameters is important factor for both process stability and filler metal distribution.

1. Introduction

Welding is a very sophisticated manufacturing process where all four states of matter are involved with rapid spatial thermal gradients resulting in weld metal with several microstructural constituents having different mechanical properties [1]. A conventional arc welding such as metal inert/active gas (MIG/MAG), tungsten inert gas (TIG) and submerged arc welding (SAW) are mainly used in many industries due to high reliability and easy automatization. A consolidation of the laser beam with arc welding, forming laser-arc hybrid welding (LAHW) originally implemented by Steen [2], has become very popular and its application is strongly rising. One of the main reasons is that the filler wire/metal is used as additional material to fill large grooves. This is particularly essential for thick sections joining and to influence the weld metal (WM) microstructure. Therefore, more favorable microstructure can be provided with enhanced mechanical properties.

The filler metal distribution in LAHW is recognized in the welding community as a potential problem. However, it has not yet received significant attention. It may be related to the fact that in conventional arc welding process with comparatively shallow penetration depths, the dilution of filler wire and base metal (BM) can be considered as homogeneous mixture in all direction within the WM. However, in the more advanced processes such as LAHW, there is high penetration depth with narrow geometry of welds. They can be termed as high-depth-to-width ratio welds. The laser beam is used to penetrate the material in keyhole mode. The filler wire from the arc source is delivered, or transported, to the weld pool and its distribution throughout the depth in narrow welds is of high concern. This commonly appears in welding of highly alloyed materials, e.g. stainless steel [3]. Analysis of filler metal distribution for such materials can be done by measuring the Cr [4] or Ni contents [5]. However, in high strength low alloy (HSLA) steels such method is difficult to implement due to small amount of alloying elements which is more difficult to quantify. Frostevarg [6] demonstrated that a discolored appearance of welds may occur after etching and filler metal distribution can be studied. However, there are limits in quantification since welding of HSLA steel is performed using filler wire with similar chemical composition as the BM. Therefore, identification of filler metal distribution in WM remains to be challenged. It is possible to use stainless steel wire for a better understanding since it will cause a strong discoloration (contrast) in the

* Corresponding author.
E-mail address: ivan.bunaziv@sintef.no (I. Bunaziv).

https://doi.org/10.1016/j.jmapro.2020.02.048
Received 24 November 2019; Received in revised form 25 February 2020; Accepted 28 February 2020

Nomenclature

a	arc weld pool width (m)
b	arc weld pool depth (m)
C	specific heat capacity ($J{\cdot}kg^{-1}{\cdot}°C^{-1}$)
c_X	front (c_f) and rear (c_r) pool length (m)
f_X	fraction of heat deposited in front (f_f = 1.5) and rear (f_r = 0.5) quadrants
H_i	heat supplied internally into a body
h	film coefficient for convection ($W{\cdot}m^{-2}{\cdot}°C^{-1}$)
I	arc current (A)
k	thermal conductivity ($W{\cdot}m^{-1}{\cdot}°C^{-1}$)
P_A	arc power output (W)
P_L	laser beam power output (W)
P_S	power of the Gaussian surface heat source (W)
q_{conv}	heat flux on a surface for convection ($W{\cdot}m^{-2}$)
q_f	front power density distribution ($W{\cdot}m^{-3}$)
q_r	rear power density distribution ($W{\cdot}m^{-3}$)
q_{rad}	heat flux on a surface for radiation ($W{\cdot}m^{-2}$)
q_H	total heat flux flowing into a body ($J{\cdot}m^{-3}$)
Q_t	total heat flux of the heat source ($W{\cdot}m^{-3}$)
r_c	radius of the cone as function depth (m)
r_e	external radius of keyhole (m)
r_i	internal radius of keyhole (m)
r_S	radius of the Gaussian surface heat source (m)
S	surface area (m^3)
T	temperature (°C)
T_0	ambient temperature (20 °C)
T_K	sink temperature (°C)
T_Z	value of absolute zero (−273.15 °C)
U	arc voltage (V)
V	volume of solid material (m^3)
v_t	welding (travel) speed ($mm{\cdot}min^{-1}$)
z	depth (vertical axis) of radius change (m)
z_e	upper keyhole plane position (m)
z_i	lower keyhole plane position (m)

Greek symbols

ε	radiation coefficient (assumed to be 0.5)
η_A	arc efficiency (assumed to be 0.8)
η_L	laser efficiency factor (assumed to be 0.7)
ρ	density of material ($kg{\cdot}m^{-3}$)
σ	Stefan-Boltzmann constant ($5.67{\cdot}10^{-8}$ $W{\cdot}m^{-2}{\cdot}°C^{-4}$)

weld metal as shown by Victor et al. [7]. However, it requires additional experimental runs and the procedure can be very costly. Another method might be to use nanoparticles, but it adds more challenges to the trial experiments and extra costs.

In the present work, longitudinal macrosections were used to assess distribution of non-metallic inclusions (NMIs) which are mainly supplied by the metal-cored filler wire in HSLA steel. Thermal gradients and melt flow behaviors were derived from prior austenite grain morphological behavior. Microstructure evolution is studied, particularly focused on acicular ferrite (AF) as the most desired constituents in weld metal for its high toughness and strength according to Svensson and Gretoft [8]. Numerical simulations were performed to understand thermal cycles at different heat inputs and depths. The proposed method is viable in assessment of deep and narrow welds. With application of automated optical microscope/SEM system and pattern recognition (based on algorithms for image analysis), the method can be extensively used in the future for the research and quality assessment in production of thick metallic sections.

2. Methodology

2.1. Experimental equipment and materials

The LAHW experiments were performed with the setup illustrated in Fig. 1a. A continuous wave of maximum 15 kW Yb:fiber laser (YLR–15000 type from IPG Laser GmbH, randomly polarized) was used through a 400 μm fiber core diameter with 1070 ± 5 nm wavelength. The beam parameter product is 14.6 mm·mrad. The focal length was 300 mm and focused spot size of 800 μm diameter, as measured, providing Rayleigh length ± 4 mm. The laser beam was inclined by a 7°30′ angle to avoid high back reflections. The MAG arc source was TPS4000 VMT Remote power source Fronius GmbH with 60° angle from the upper plate surface. The MAG source had ability to make reciprocating motion of the wire which provides the cold metal transfer CMT arc mode.

The constant process parameters employed were: 15 kW laser beam power, −7 mm focal point position (*FPP*), 15 ± 1 mm filler wire stick-out, 4 ± 0.5 mm distance between laser and arc sources or process distance (D_{LA}), 82 % Ar + 18 % CO_2 shielding gas composition with 25

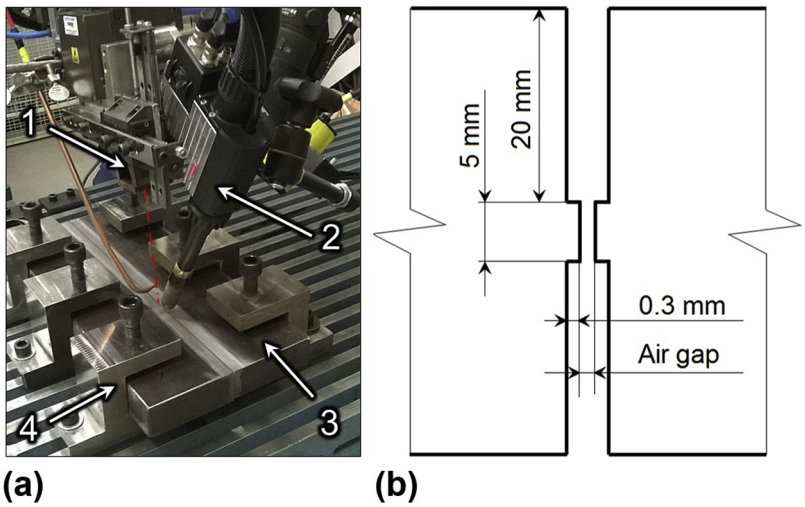

Fig. 1. (a) Experimental equipment: 1 – laser beam head; 2 – MAG torch; 3 – specimens; 4 – clamping system. (b) Groove geometry preparation.

L·min^{-1} shielding gas flow, pulsed arc mode, and trailing arc position (when laser is leading). No back shielding was applied.

The base metal used was 45 mm thick microalloyed HSLA steel. Its yield ($R_{p0.2}$) and ultimate tensile strength (R_m) is 522 and 629 MPa, respectively. The plates were cut to 500 × 120 × 45 mm^3 specimen size. During welding, the specimens were heavily clamped to the table with the fixture to ensure consistent air gap size. An I-groove geometry with 5 mm root face in the middle (see Fig. 1b) was used with milled edges having low roughness (R_a = 1.6 μm). The top surface of the plates was sandblasted to remove ferrous surface oxides such as FeO/Fe_2O_3/Fe_3O_4 [9], and corrosion products, and to secure laser from high back reflections. In this work, it is assumed that sand residuals such as quartz and silicates do not influence inclusions in the WM.

Metal-cored filler wire was used with 1.2 mm in diameter. The chemical composition of the BM and filler wire is outlined in Table 1. The nominal weld metal yield ($R_{p0.2}$) and tensile strength (R_m) is 518 MPa and of 598 MPa, respectively.

2.2. Experimental procedure

Welding was performed from both sides using the parameters presented in Table 2. One of the experiments (Weld No. 1) is taken as a reference weld. Then, the effects of increased air gap and welding speed were studied. The filler wire feed rate (*WFR*) was adjusted depending on the actual air gap to avoid underfilling in thick section welding. For the purpose of comparison, one experiment (Weld No. 2) with different arc mode was also included (CMT + P). For understanding the filler metal transporting capability to the root area, the change of *WFR* has lower importance due to high power of the laser beam used and high depth-to-width morphology of the welds. In addition, the effect of several process variables can be studied within a limited number of test runs. The synergetic program for the arc part was used to provide stable processing by a controlled filler wire melting depending on its feeding rate used.

The total line energy input for LAHW (Q_H, kJ·mm^{-1}) can be calculated by summation of the laser beam energy input (Q_L, kJ·mm^{-1}) and the arc energy input (Q_A, kJ·mm^{-1}):

$$Q_H = Q_L + Q_A = \frac{60 \cdot P_L \cdot \eta_L}{1000 \cdot v_t} + \frac{60 \cdot P_A \cdot \eta_A}{1000 \cdot v_t} \quad (1)$$

2.3. Analysis of NMIs, microstructure and hardness

In this work, a longitudinal cut (see Fig. 2) along the weld centerline is studied. A minimum length of the weld was set to be 65–70 mm (Weld No. 3), which is sufficiently to provide reasonable studies with high reliability and cost-efficiency. Most of the weld imperfections in deep and narrow welds are concentrated at the centerline, thus it can also reveal their position and morphology for the further study. X-ray radiography and ultrasonic detection are limited since they mainly can detect imperfections of a certain size (pores, cracks) while small pores/cracks may be undetected. Non-etched (as polished) samples were studied by scanning electron microscope (SEM) with a backscattering detector (to enhance contrast) to accurately characterize NMIs (their density and size) and etched sample were used for microstructure evaluation. To cover a whole weld metal area requires many images to be processed. Therefore, a special procedure was developed and shown in Fig. 2b. Three SEM images were taken from the same place for each weld at different columns and depths. One base metal sample was included for comparison. The average size and numbers of NMIs and the morphological features of AF were analyzed by *FIJI* software (*ImageJ*) [10].

The samples were etched with 2% Nital for 30 s to identify the various microstructure constituents and physical filler metal distribution along the weld centerline.

The Vickers hardness test was performed based on EN ISO 9015–1 in accordance with ISO 6507–1. The selected load was HV_{10} (corresponding to 10 kg) for longitudinal cuts.

2.4. Numerical simulation

The process was numerically simulated in ABAQUS/Standard, where the DFLUX subroutine was used to introduce a moving heat source.

A thermal analysis of LAHW was performed to estimate thermal history and cooling rates in the areas of interest. The non-linear transient heat transfer analysis (here the Lagrangian description is assumed) is obtained by solving equation where the energy balance (Green-Naghdi type) with combined Fourier law obtained directly by the standard Galerkin approach within spatial discretization [11]:

$$\int_V \rho C \Delta T dV + \int_V \frac{\partial \Delta T}{\partial (x, y, z)} \cdot k \cdot \frac{\partial T}{\partial (x, y, z)} dV = \int_V \Delta T H_i dV + \int_S \Delta T Q_t dS \quad (2)$$

The model applied contained DC3D8 (8-node brick) and DC3D4 (4-node tetrahedron, for transition zone between coarse mesh and fine mesh towards the weld centerline) first order isoparametric continuum linear elements. In total 207 356 elements were used with 0.7 mm^3 size in active zone near the weld centerline.

The specific heat capacity and thermal conductivity applied in the model were assumed to be temperature-dependent (see Fig. 3) to include the effect of the ferrite-austenite transformation according to Sun et al. [12].

Other material properties used in numerical estimation were density (for solid phase 7800 kg·m^{-3}, for liquid phase 6800 kg·m^{-3}), solidus point (1450 °C), liquidus point (1530 °C), and latent heat of fusion (250 000 J·kg^{-1} °C^{-1}) due to phase transformation (liquid-solid) which is very important for accuracy of the model according to Karkhin et al. [13].

The LAHW process was simulated as a combination of three combined heat sources $Q_H = Q_1$ (conical laser source) + Q_2 (ellipsoidal arc source) + Q_3 (the Gaussian surface source).

The laser keyhole is represented through a body flux as the conical volumetric heat source (Q_1, W·m^{-3}) provided by the following equation [14]:

$$Q_1 = \frac{9\eta_K Q_L}{\pi(1 - e^{-3})} \frac{1}{(z_e - z_i)(r_i^2 + r_e r_i + r_e^2)} \exp\left[-\frac{3(x^2 + y^2)}{r_c^2}\right] \quad (3)$$

$$r_c(z) = r_e + \frac{r_i - r_e}{z_i - z_e}(z - z_e) \quad (4)$$

For the arc source (Q_2, W·m^{-3}), the Goldak double ellipsoidal volumetric heat source was used [15]. The heat source is comprising of front (q_f when $y < y_0$) and rear (q_r when $y \geq y_0$) power density distribution quadrants [16]:

Table 1
Material chemical compositions, representing wt.%.

Material	C	Si	Mn	P	S	V	Ni	Cu	Mo	Fe
BM	0.036	0.082	1.97	0.007	0.001	0.01	0.70	0.18	0.1	Bal.
Wire	0.060	0.350	1.41	0.011	0.017	< 0.05	1.48	< 0.30	< 0.20	Bal.

Table 2
Process parameter table.

Weld No.	v_t, m·min^{-1}	Air gap, mm	*WFR*, m·min^{-1} (current/voltage)	Q_A, kJ·mm^{-1}	Q_L, kJ·mm^{-1}	Q_H, kJ·mm^{-1}
1	0.6	0.4	7 (188/28.6)	0.43	1.05	1.48
2	0.6	0.6	7 (137/19.0)*	0.21	1.05	1.26
3	0.8	0.3	9 (223/28.9)	0.38	0.79	1.17
4	0.8	0.8	10 (256/28.6)	0.44	0.79	1.23
5	1.2	1.0	18 (379/34.1)	0.52	0.53	1.05

* CMT + P arc mode was used.

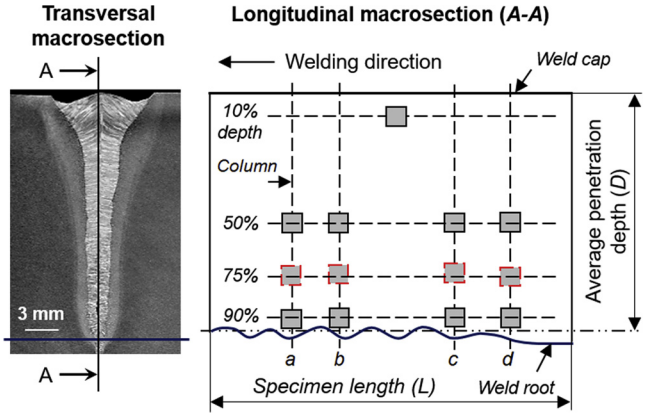

Fig. 2. Analysis method of NMIs in longitudinal macrosection indicating areas of inspection.

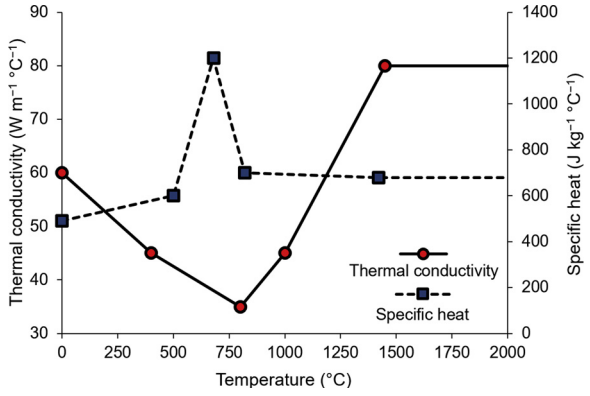

Fig. 3. Temperature-dependent variation of specific heat capacity and thermal conductivity of HSLA steel.

$$Q_2 = q_f + q_r = \frac{6\sqrt{3} f_X UI\eta_A}{abc_X \pi\sqrt{\pi}} \exp\left(-\frac{3x^2}{c_X^2}\right)\exp\left(-\frac{3y^2}{a^2}\right)\exp\left(-\frac{3z^2}{b^2}\right) \quad (5)$$

In addition to conical and Goldak double ellipsoidal heat sources, the Gaussian surface heat flux was applied to approach similar weld geometry in the upper part. The conical heat source does not provide appropriate width in the upper part due to its nature and heat convection being neglected. The Gaussian surface heat flux (Q_3, W·m^{-2}) is described by the following equation [17]:

$$Q_3 = \frac{2P_S}{\pi r_S^2} \exp\left[-\frac{2(x^2 + y^2)}{r_S^2}\right] \quad (6)$$

The initial boundary condition is defined by setting the temperature of the specimens to 20 °C. Natural heat convection (Eq. 7) and heat radiation (Eq. 8) losses were applied to the surfaces [11]:

$$q_{conv} = -h(T - T_K) \quad (7)$$

$$q_{rad} = \varepsilon\sigma[(T - T_Z)^4 - (T_0 - T_Z)^4] \quad (8)$$

3. Results and discussion

3.1. Processing stability

The transversal and longitudinal macrosections of weld are presented in Fig. 4a-e. The top weld surface had a slight waviness (in longitudinal direction) and it was excluded from studies due to low relevance. The longitudinal macrosection is very informative in understanding of variation in penetration depth and root morphology compared to transversal macrosection, the cut location was presented in Fig. 2. In most cases, welds had incomplete penetration with variation in maximum penetration with waviness.

In case of Weld No. 5 (Fig. 4e), full penetration was achieved in most of the length. Consequently, transversal macrosections do not consistently reveal a *true* penetration depth over the length. However, average values are very similar to measured values from random transversal macrosection (which were taken from the end of welds) in the range of ± 0.3 mm deviation for all studied welds. The change in penetration depth over the weld length is uniform. An exception is Weld No. 1 (Fig. 4a), where depth is slightly reduced with processing time. This observation is possibly due to decrease in air gap between the plates or related to specific welding condition with other process parameters. Modern fiber lasers provide very stable maximum power level, and variation in penetration depth over the weld length may be related to the periodic characteristic of the molten phase transport at the keyhole front wall. It can also be attributed to weld plume fluctuations. These also concern 1070 nm wavelength lasers at high power levels where the beam can be partly absorbed by the weld plume [18]. The thermal fluid flows from the keyhole front wall through the bottom of the keyhole root as a melt bridge (just under the keyhole). It is well known that fluid flow at the bottom bridge is 3–10 times faster than at the rear part of weld pool [19] depending on the process parameters. This may be a possible explanation of variation in penetration depth. A periodic transfer of molten metal in discreet portions from the front keyhole wall through the keyhole bottom to the rear weld pool which has a high dynamic influence causing eddy and unstable fluid flow patterns from the bottom towards the plate surface. Another explanation of depth variation can be due to high frequency of fluctuations/oscillations of the vapor filled capillary in real time [20]. In addition, Zhang et al. [21] showed that there is an uneven distribution of laser energy at the keyhole wall and variation of keyhole radius even in quasi steady-state processing. This indicates a noticeable and complex variation in penetration depths.

In the case of air gap overfill, a *saw-tooth* geometry pattern is resembled when partial penetration occurs, as shown in Fig. 4b-d. The cyclic or discrete characterization of the root morphology (its curvature) is random and not dependent on process variables within the selected range. For double-sided welding technique, such a periodic molten metal overfilling is harmful in order to maximize process efficiency. As a result, the second weld must penetrate into the first weld in order to achieve a sound weld. In this case, a second pass with higher penetration depth by using high power of the beam can be less stable causing porosity and additional heat input with higher distortions.

The process stability and resulting porosity is clearly seen from longitudinal macrosections. Porosities were predominantly located at

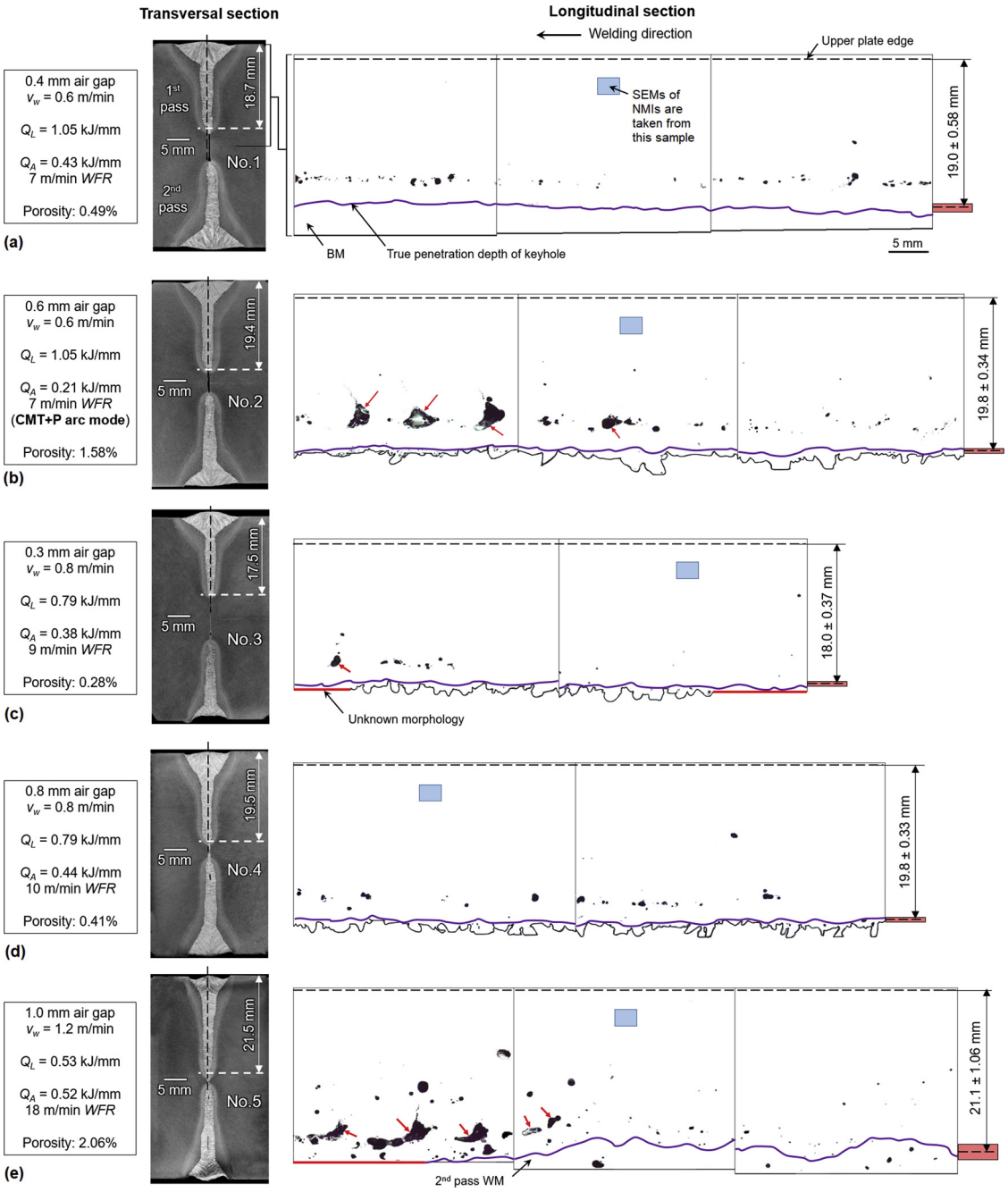

Fig. 4. Internal imperfection and root morphology based on longitudinal cuts alinged with the first pass at weld centerline.

75 % depth (Fig. 4a-e). Most of the pores had spherical geometry. The main mechanism of porosity generation is related to the rear keyhole wall behavior. Kaplan [22] observed that the front wall has the primary responsibility since it first absorbs the incident laser rays. The vaporization conditions (e.g. angle of incidence, delivered laser beam power) have a profound effect on the dynamic stability of the rear keyhole wall during multiple reflections, the Fresnel absorption, of the trapped laser light. Similar model and assumptions were recently confirmed by Kouraytem et al. [23]. Eriksson et al. [24] showed that the molten metal velocities at the front keyhole wall can reach > 10 $m{\cdot}s^{-1}$ by applying > 10 kW laser power. As a result, the waviness of the walls is significant, especially at the bottom or the root area. This causes an increase of absorption of the incident laser beam, at grazing angles of 3–7° [25], along subsequent uneven vaporization with excessive evaporation of metal (Fig. 5a). This may, in turn, form the metal vapor filled pocket at the rear keyhole wall due to critically high deformation force/recoil pressure related to very high local absorptivity of the laser beam (indicated by area *A* in Fig. 5b) with preferable Brewster angle. Hereafter, the bubble formed filled with plasma vapor detaches from the weld pool. Similar mechanism was numerically predicted [26] showing large formation of bulges at the rear keyhole wall. The deformation of the rear keyhole surface was experimentally shown by Jian et al. [27]. At the same time, Zhang et al. [28] showed similar results where the steel/glass sandwich technique was applied. At faster welding speeds, the keyhole is more inclined (as shown in Fig. 5b); this will provide higher laser beam absorption with increased pressure (or the shockwave of plasma) and larger deformation of the rear keyhole wall. Similar behavior was experimentally observed by Li et al. [29]. It can be a reason for higher porosity at 1.2 $m{\cdot}min^{-1}$ welding speed and possibly complete keyhole collapse.

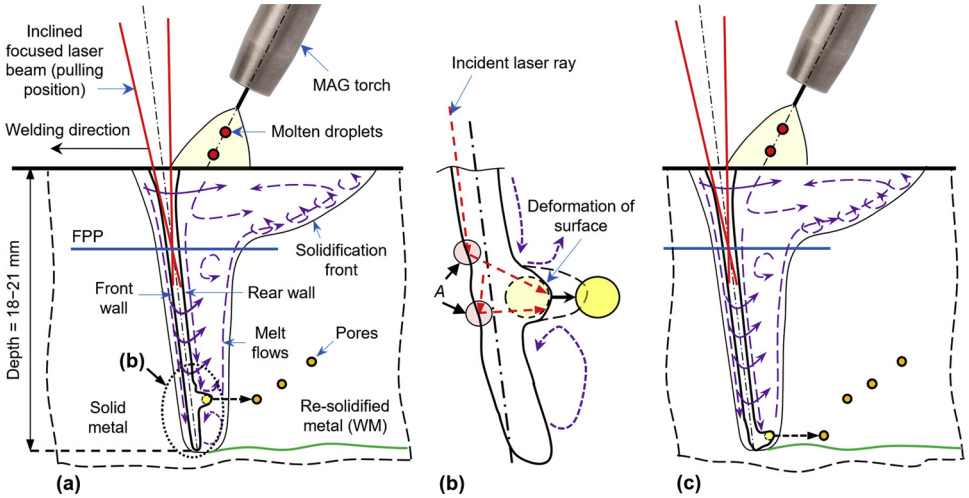

Fig. 5. Keyhole dynamics and porosity generation mechanism at (a) 75 % penetration depth with (b) simplified physical model of pore cavity formation by deformation of rear keyhole wall and in (c) root 90–95 % depth.

There is low tendency of porosity at 90–95 % depth except Weld No. 5. These can be generated by molten metal overflow and subsequent keyhole collapse, illustrated in Fig. 5c. At deeper part of keyhole, the process is more unstable and turbulent melt flows seem to occur due to increased welding speed. Since larger air gap between the plates was used, melting of edges can cause more unstable melt flow conditions at any depth.

Pores observed at lower depth near the plate surface (< 50 % depth) may origin from pores generated at 75 % depth. These were driven by the melt flows (shown in Fig. 5a) with much longer solidification rate of the molten metal due to slower cooling time (see Section 3.3).

Large (gas) cavities are shown in Fig. 4b,c,e (by red arrows); these had small thickness (0.1–0.2 mm) in transversal direction. This observation indicates that such cavities may be solidification cracks since they are clearly visible on transversal macrosections within the same depth location. Therefore, such solidification cracks might occur mainly due to unfavorable melt flow dynamics in combination with high solidification rates (cooling times at different depths are presented later in Section 3.3) and complete keyhole collapses. Application of CMT + P arc mode (Weld No. 2), also exhibited large gas cavities. This may be related to unstable droplet transfer where *wire chopping* instability causing keyhole collapses by chopped filler wire which frequently strikes keyhole opening areas [30]. As a result, large gas cavities are mainly generated due to highly unstable processing conditions which also might represented solidification cracks or hot tearing phenomena.

3.2. Grain behavior

Depending on the process variables, different prior austenite grain (PAG) morphology can be recognized based on longitudinal macrosections and shown in Fig. 6. In the upper part (zone *i*), columnar PAGs are generated primarily at 80–90° direction (perpendicular to welding direction). In the middle of the weld metal (zone *ii*), equiaxed PAGs are dominant. At the root (zone *iii*), columnar PAGs are curved at −60° direction. Approximately at 75 % depth, a more complex behavior of

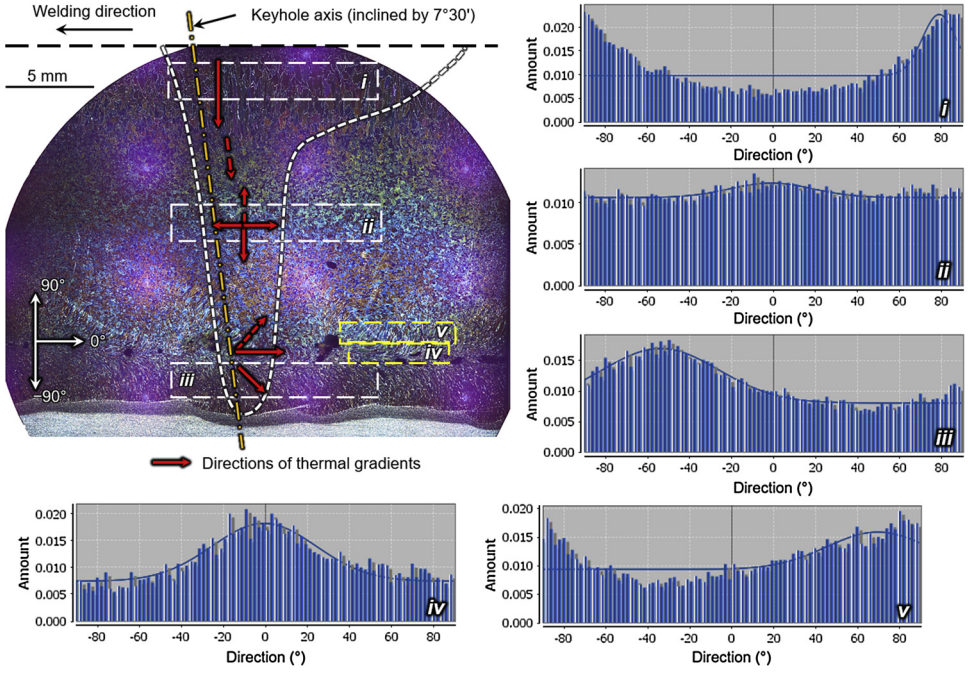

Fig. 6. Behavior of grains in logitidunal macrosection of welds. Meaning of *i-v* areas is explained in the text.

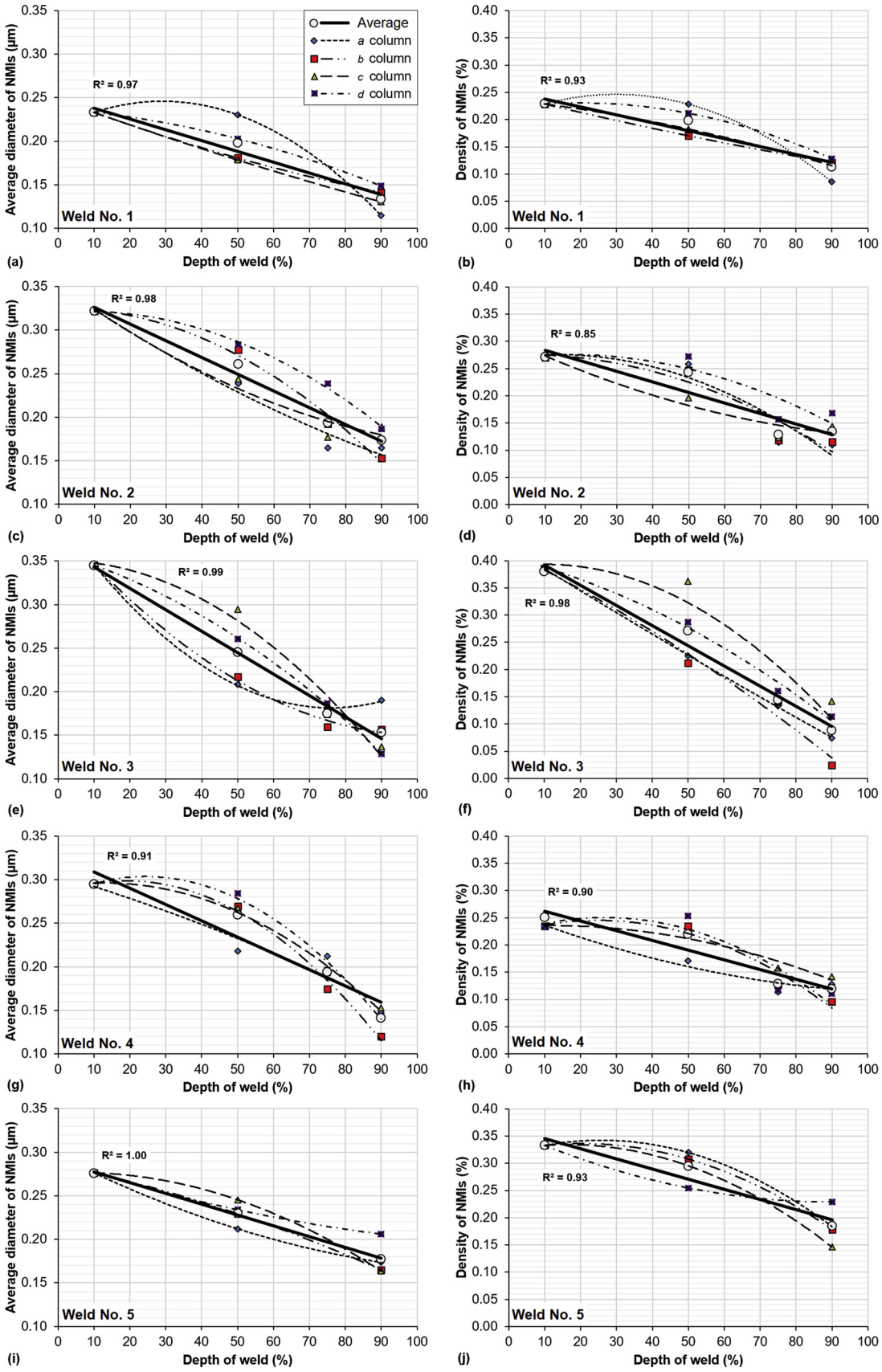

Fig. 7. Statistical characterization of NMIs for individual weld sample.

the PAGs is recognized falling mostly between −20° and 20° directions (zone *iv*). Slightly above this zone (zone *v*) the direction was mainly at 60° indicating upward melt flows from the root. Based on the morphology of PAGs, thermal gradients can be identified. Thermal gradients may be directly correlated to fluid flow during processing. Based on the longitudinal macrosections in Fig. 4, the turbulent fluid flow coincides with grain orientation (thermal gradients) in the same zones, which is 75 % penetration depth. Such fluid flow behavior might be responsible for porosity generation.

3.3. Statistical characterization of the NMIs

Statistical characterization of NMIs based on SEM is represented in Fig. 7 for different penetration depths. The filler metal distribution can be recognized based on the density (or volume fraction) of NMIs since the BM has much less amount of NMIs. This is the main reason why conventional high strength low alloy steels cannot nucleate AF and usually consist of the mixture of ferrite and bainite.

For the individually selected areas in term of vertical line (the column through thickness, see Fig. 2), a second polynomial trend line was used. For the whole sample, including all columns with averaged results, a linear trend line had the best fitting. Regardless of the column, there is linear trend with a high coefficient of determination $R^2 > 0.95$. As a result, there is a linear decrease of density of NMIs (their number and size based on SEM images) or decrease of filler metal portion towards the root. Moreover, by averaging all results (see Fig. 8), regardless of welding parameters, there is a strong linear correlation between diameter and density of NMIs with increase of weld depth. However, some welds showed poor correlation especially for individual inspection columns where a second-degree polynomial fitting was used, with some scatter in results. This finding indicates that filler metal distribution has wavy or heterogeneous distribution in respect to the depth in the WM and will be shown later.

To understand such behavior, thermal cycles were extracted from numerical simulations where comparison with experimental trials is presented in Fig. 9. Cooling times from 800 to 500 °C, denoted as $\Delta t_{8/5}$, is compiled based on penetration depth (see Fig. 10). Based on Figs. 8 and 10, the average diameter of NMIs and density shows similar decreasing trend as cooling time. However, for Weld No. 5, at larger depths, the cooling rate has higher gradient and hence poorer correlation. Thus, in this case, 3rd degree polynomial trendline shows stronger correlation. It may be related to narrower joint geometry at the upper part. In the root, welds had similar fast cooling time regardless heat input used. As a conclusion, the average diameter of NMIs is evidently affected by the cooling time. This observation is in agreement with the previous results have shown that the NMI size depends on the heat input [31].

3.4. Microstructure

The volume fraction of AF for different depths is presented in Fig. 11. All welds (except Weld No. 5) had a gradual reduction in AF towards the root (excellent agreement with second order polynomial trend curve $R^2 = 0.99$ and good linear trend with $R^2 = 0.90$). It has similar trend with cooling time (see Fig. 10) and seems to be directly dependent. Weld No. 5 had more rapid decrease of AF at depth > 50 % but still had a good correlation with second order polynomial $R^2 = 0.93$ and linear fitting $R^2 = 0.90$. Therefore, for the latter case, a more complex non-linear fitting curve may be more optimum with a steep decrease of NMIs at 50 % depth, e.g. sigmoid function type.

By SEM inspection, the upper part, or arc zone, mainly consisted of very fine interlocked AF (Fig. 12a) with high misorientation angles (Fig. 12b), which is normally connected to high crack arrest property [33]. In the root, the AF morphology was very different from that found in the upper zones depending on the cooling time (heat input). In case of high heat input, AF had larger platelets (Fig. 13a) inherently providing lower mechanical properties. However, high misorientation angles were maintained (Fig. 13c). Bainite was frequently observed and its morphology resembles granular bainite. For lower heat input with very short cooling time, AF platelets were significantly elongated (Fig. 13b), as intragranular Widmanstätten ferrite (IWF) [34], with the specific orientations (Fig. 13d). As a result, such behavior will provide lower mechanical properties. In addition, lath martensite was observed in substantial quantities but not exceeding 20 % of volume fraction. In agreement with the lower volume fraction of NMIs in the root, the volume fraction of IWF is higher, i.e., in the range from 5 to 15 %.

3.5. Filler metal distribution and hardness

The amount of filler metal transported to the root and corresponding dilution can be understood based on the density of NMIs. In the root, the amount of filler metal is only half of that found in the upper part (see Fig. 8). This implies that BM dilution is high (more fused base metal in WM), providing a lower AF volume fraction. However, based on the filler wire chemical composition, high density of NMIs can also provide low AF formation [35] when the cooling rate is high enough.

The use of numerical simulation to predict filler metal mixing can open a new possibility to reduce expensive experimental runs and post-weld inspection [36]. However, the application of computational fluid dynamics related to very complex LAHW with long calculation time and the accuracy of results is under concern due to oversimplification of the model. Moreover, an accurate comparison with real keyhole dynamics is not published since deep penetration laser welding is challenging to observe. Application of transparent glass to metal, called as sandwich technique [28,29,37,38], changes the density of fluid and only partially explain some phenomena. In addition, tracing particles are challenging

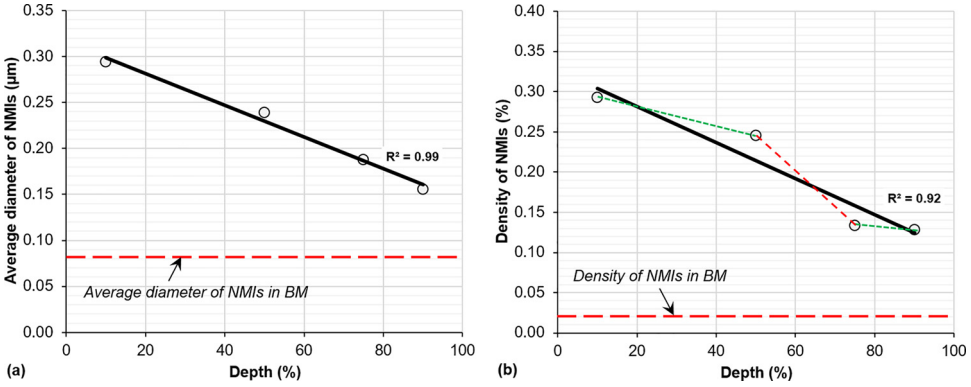

Fig. 8. Averaged statistical characterization of NMIs.

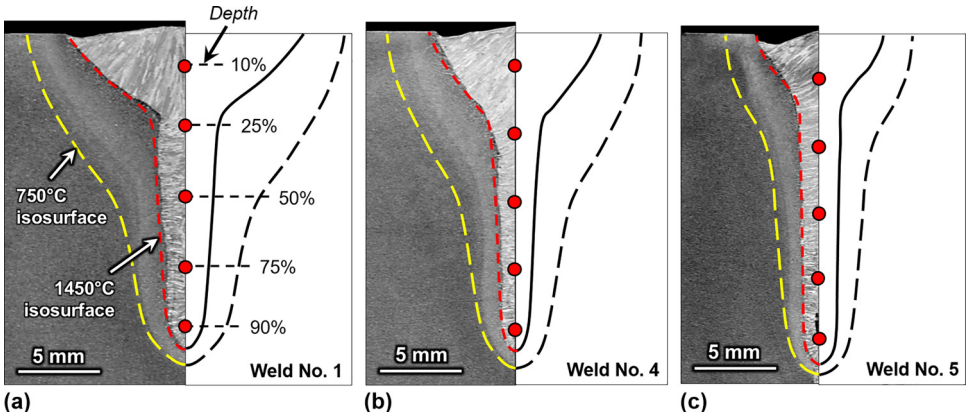

Fig. 9. Numerical simulation results of (a) Weld No. 1, (b) Weld No. 4, and (c) Weld No. 5.

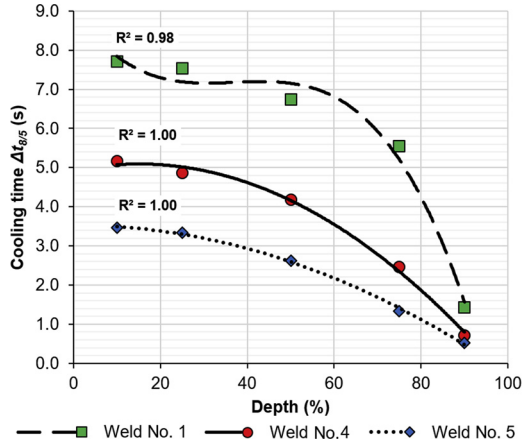

Fig. 10. Numerically estimated cooling times ($\Delta t_{8/5}$) in weld metal according to depth.

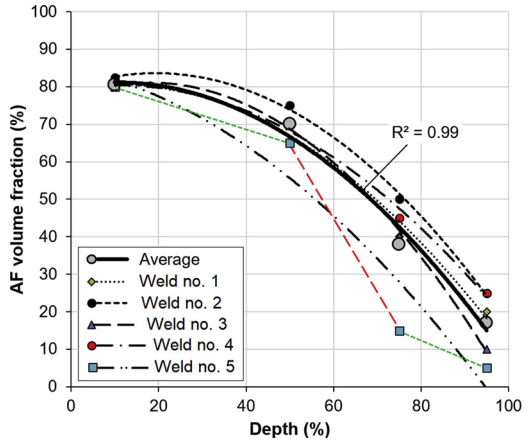

Fig. 11. AF volume fraction at different depths. Data adopted and modified from [32].

to detect when high melt velocities and complex physics are involved [39].

By inspection of longitudinal macrosections, a clear discoloration is visible (as contrast). A schematic discoloration with enhanced contrast is presented in Fig. 14. To understand such behavior, NMIs were studied at the borders of discoloration zones (inspected areas are shown in Fig. 14b by red rectangular). The density of NMIs is significantly different and a higher density is present in darker discolored areas. The darker area had a density of 0.28 %, while outside the region the density was 0.17 %. These results are very similar to the statistical data

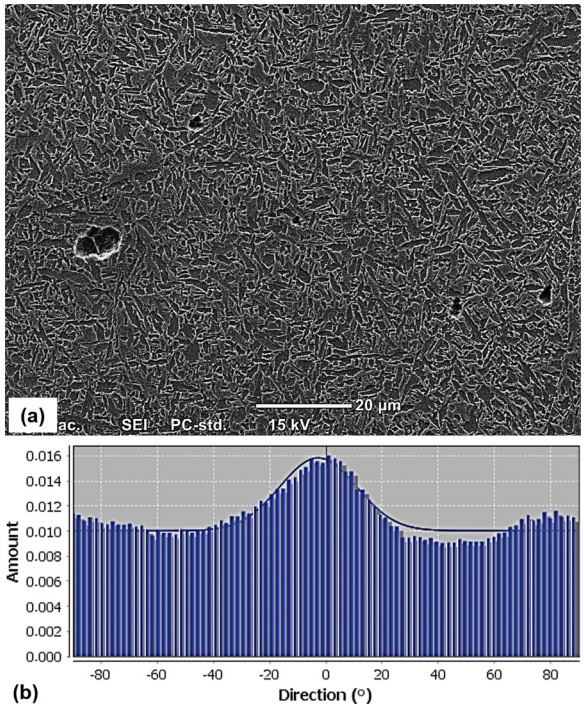

Fig. 12. (a) SEM image of fine-grained AF and (b) misorientation angles in Weld No. 5 in upper zone showing equiaxed behavior.

of NMIs presented in Fig. 9. This observation strongly indicates that the distribution of NMIs and filler metal is inhomogeneous both in the longitudinal and the vertical directions. With small air gap and low welding speed, the filler metal seems to be distributed by the saw-tooth pattern (Fig. 14a–c).

At larger air gaps and high welding speeds, the direction of the saw-tooth pattern is opposite and is very unsteady. Weld No. 5 (Fig. 14e) has low filler metal transportation ability even with larger air gap compared to other experimental runs, but welding speed was higher and caused unstable fluid flow in the weld pool.

The hardness results measured in longitudinal direction at different depths are shown in Fig. 15a and c for low and high heat input, respectively. Hardness indentations were made with 2.0 × 1.5 mm^2 grid size with lower number of indents in the upper part since the microstructure is more homogenous in that area (see Fig. 11) with expected uniform hardness level. The hardness data was processed in *Python* via interpolation with the Delaunay triangulation (Matplotlib library *v3.1.1* [40] and and NumPy library). Lower hardness was achieved with higher heat input (mainly from the laser beam), which is consistent

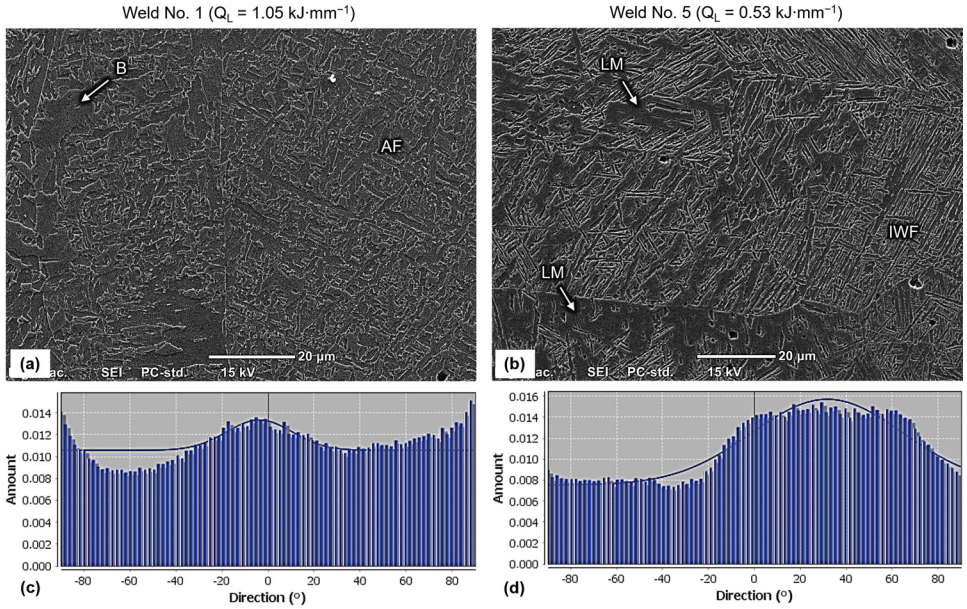

Fig. 13. SEM of microstructure and misorientation angles in root of (a,c) high heat input and (b,d) low heat input welding.

with slower cooling rate (see Fig. 10). There is a clear indication of rapid hardness increase towards the root (based on 2nd degree polynomial fitting) where more steep hardness increase is obtained at larger depth (> 80 % of total depth). Up to 50–60 % depth, the hardness follows a linear increase. Based on hardness mapping shown in Fig. 15b and d for low and high heat input respectively, there is a clear evidence of hardness variation along the longitudinal direction, and it seems to follow the discoloration phenomenon due to the filler metal mixing. Moreover, it seems that the filler metal also tend to reduce hardness values due to higher AF formation which can be visible from Fig. 15b,d. This implies that hardness is not only affected by the heat input but also by various process parameters that control the filler metal distribution. As a result, lower welding speeds may not only give higher heat input and potentially improved penetration depths, but also provide better filler metal mixing and process stability, as discussed in Section 3.1.

4. Conclusions

In the present study, LAHW of thick plates have been used with metal-cored wire. Based on the experimental observations, the conclusions can be drawn as follows:

- Deep penetration laser-arc hybrid welding has inconsistent penetration depth related to process stability and sensitivity. Therefore, longitudinal macrosections should be examined to understand welding of thick plates, in addition to the more traditional

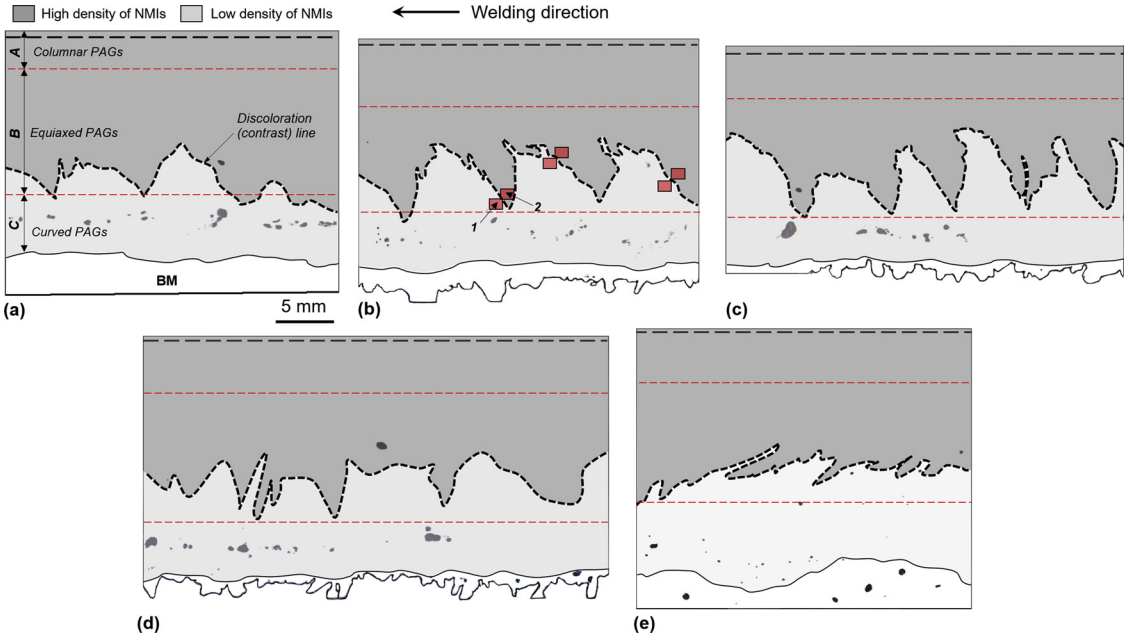

Fig. 14. Physical filler metal distribution maps with rapid transition from high to low density of NMIs in longitudinal macrosections after etching based on discolored pattern in weld metal: (a) Weld No. 1; (b) Weld No. 2; (c) Weld No. 3; (d) Weld No. 4; and (e) Weld No. 5. *A* – zone depth of columnar PAGs, *B* – zone depth of equiaxed PAGs, *C* – zone depth of curved PAGs. Red squares represent the examined areas where *1* – inspection for low density of NMIs and *2* – area of inspection for high density of NMIs (For interpretation of the references to colour in this figure legend, the reader is referred to the web version of this article).

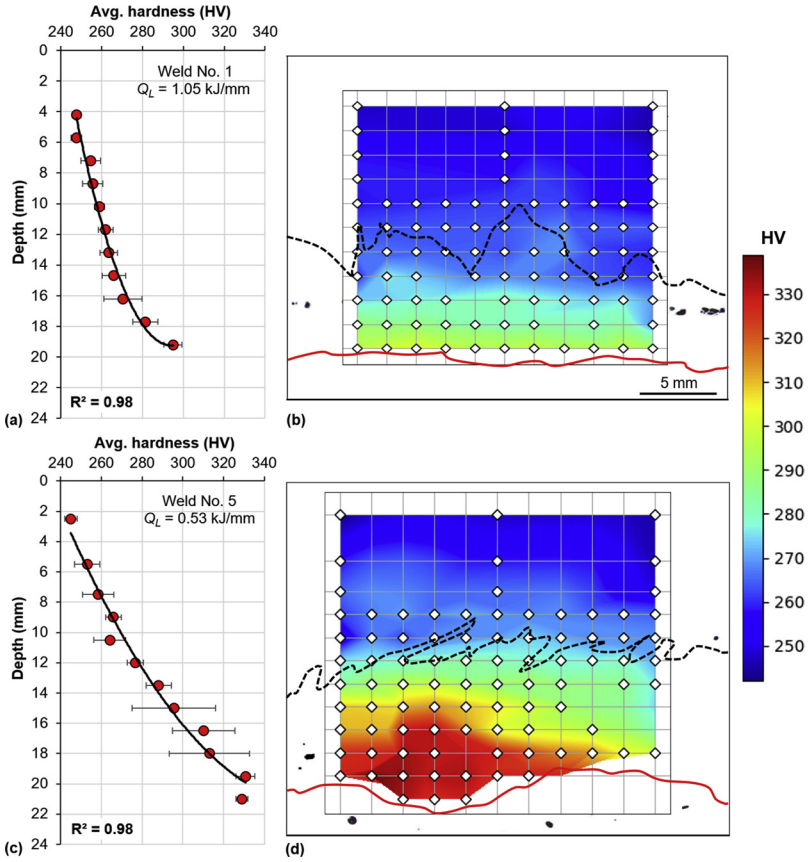

Fig. 15. Hardness distribution maps in LAHW with (a,b) high heat input (Q_L = 1.05 kJ·mm^{-1}) and (c,d) low heat input weld (Q_L = 0.53 kJ·mm^{-1}). (a,c) shows average hardness values at certain depth and (b,d) individual hardness values distributed on longitudinally cut specimen at weld centerline (For interpretation of the references to colour in this figure legend, the reader is referred to the web version of this article).

transversal cross weld macros.

- In the root area, the fraction of the transported filler metal is substantially lower compared to the upper part of weld. This may lower mechanical properties due to an associated reduction of the acicular ferrite volume fraction.
- An increase of air gap provides enhanced filler metal transportation to the root area at slower welding speeds (< 1.0 m min^{-1}). At faster welding speed, the weld pool is unstable and has low efficiency in filler metal transportation.
- Longitudinal cuts may disclose more features concerning weld defects and prior austenite grain morphology. Moreover, NMIs and filler metal distribution may be readily visible after etching.
- The heat input from the laser beam has significant influence on the weld metal hardness. The hardness varies both in the longitudinal and vertical directions, and transverse cross sectioned macros may thus provide unreliable interpretation of mechanical properties of welds.

Declaration of Competing Interest

The authors declare that they have no known competing financial interests or personal relationships that could have appeared to influence the work reported in this paper.

Acknowledgements

The authors wish to thank the Research Council of Norway for funding through the Petromaks 2 Programme, Contract No. 228513/E30. The authors acknowledge funding from the EC Research Fund for Coal and Steel, RFCS, project OptoSteel, No. 709954. The financial support from ENI, Equinor, Lundin, Total, JFE Steel Corporation, Posco, Kobe Steel, SSAB, Bredero Shaw, Borealis, Trelleborg, Nexans, Aker Solutions, FMC Kongsberg Subsea, Marine Aluminium, Hydro and Sapa are also acknowledged.

References

[1] Bhadeshia HKDH, Honeycombe RWK. Steels: microstructure and properties. 3rd ed. Butterworth-Heinemann; 2006.
[2] Steen WM. Arc augmented laser processing of materials. J Appl Phys 1980;51:5636–41.
[3] Gook S, Gumenyuk A, Rethmeier M. Hybrid laser arc welding of X80 and X120 steel grade. Sci Technol Weld Join 2014;19:15–24.
[4] Karhu M, Kujanpää V, Eskelinen H, Salminen A. Filler metal mixing behaviour of 10 mm thick stainless steel butt-joint welds produced with laser-arc hybrid and laser cold-wire processes. Appl Sci 2019;9:1685.
[5] Meng X, Bachmann M, Artinov A, Rethmeier M. Experimental and numerical assessment of weld pool behavior and final microstructure in wire feed laser beam welding with electromagnetic stirring. J Manuf Process 2019;45:408–18.
[6] Frostevarg J. Comparison of three different arc modes for laser-arc hybrid welding steel. J Laser Appl 2016;28:022407.
[7] Victor B, Nagy B, Ream S, Farson D. High brightness hybrid welding of steel. 28th International Congress on Applications of Lasers and Electro-Optics (ICALEO). 2009. p. 79–88.
[8] Svensson LE, Gretoft B. Microstructure and impact toughness of C-Mn weld metals. Weld J 1990;69:454–61.
[9] Fursey A. Oxide films on mild steel. Nature 1965;207:747–8.
[10] Schindelin J, Arganda-Carreras I, Frise E, Kaynig V, Longair M, Pietzsch T, et al. Fiji: an open-source platform for biological-image analysis. Nat Methods 2012;9:676–82.
[11] SIMULIA. Abaqus analysis user's manual 6.14. 2014.
[12] Sun J, Hensel J, Klassen J, Nitschke-Pagel T, Dilger K. Solid-state phase transformation and strain hardening on the residual stresses in S355 steel weldments. J Mater Process Technol 2019;265:173–84.
[13] Karkhin VA, Ilin AS, Pesch HJ, Prikhodovsky AA, Plochikhine VV, Makhutin MV, et al. Effects of latent heat of fusion on thermal processes in laser welding of aluminium alloys. Sci Technol Weld Join 2005;10:597–603.
[14] Zain-ul-Abdein M, Nelias D, Jullien J-F, Deloison D. Prediction of laser beam welding-induced distortions and residual stresses by numerical simulation for aeronautic application. J Mater Process Technol 2009;209:2907–17.
[15] Goldak J, Akhlaghi M. Computational welding mechanics. Springer; 2005.
[16] Aarbogh HM, Hamide M, Fjær HG, Mo A, Bellet M. Experimental validation of finite element codes for welding deformations. J Mater Process Technol 2010;210:1681–9.
[17] Tran H-C, Lo Y-L. Heat transfer simulations of selective laser melting process based

on volumetric heat source with powder size consideration. J Mater Process Technol 2018;255:411–25.
[18] Shcheglov PY, Gumenyuk AV, Gornushkin IB, Rethmeier M, Petrovskiy VN. Vapor–plasma plume investigation during high-power fiber laser welding. Laser Phys 2013;23.
[19] Grigoryants AG, Shiganov IN, Misyurov AI. Technological processes of laser treatment. Moscow: Bauman MSTU; 2006.
[20] Volpp J, Vollertsen F. Modeling keyhole oscillations during laser deep penetration welding at different spatial laser intensity distributions. Prod Eng 2015;9:167–78.
[21] Zhang LJ, Zhang JX, Gumenyuk A, Rethmeier M, Na SJ. Numerical simulation of full penetration laser welding of thick steel plate with high power high brightness laser. J Mater Process Technol 2014;214:1710–20.
[22] Kaplan A. A model of deep penetration laser welding based on calculation of the keyhole profile. J Phys D Appl Phys 1994;27:1805–14.
[23] Kouraytem N, Li X, Cunningham R, Zhao C, Parab N, Sun T, et al. Effect of laser-matter interaction on molten pool flow and keyhole dynamics. Phys Rev Appl 2019;11:064054.
[24] Eriksson I, Powell J, Kaplan AFH. Melt behavior on the keyhole front during high speed laser welding. Opt Lasers Eng 2013;51:735–40.
[25] Matti RS, Kaplan AFH. Post-modelling of images from a laser-induced wavy boiling front. Appl Surf Sci 2015;357:2277–84.
[26] Ai Y, Jiang P, Wang C, Mi G, Geng S. Experimental and numerical analysis of molten pool and keyhole profile during high-power deep-penetration laser welding. Int J Heat Mass Transf 2018;126:779–89.
[27] Jiang M, Chen X, Chen Y, Tao W. Increasing keyhole stability of fiber laser welding under reduced ambient pressure. J Mater Process Technol 2019;268:213–22.
[28] Zhang D, Wang M, Shu C, Zhang Y, Wu D, Ye Y. Dynamic keyhole behavior and keyhole instability in high power fiber laser welding of stainless steel. Opt Laser Technol 2019;114:1–9.
[29] Li S, Chen G, Zhang Y, Zhang M, Zhou Y, Deng H. Investigation of keyhole plasma during 10 kW high power fiber laser welding. Laser Phys 2014;24:106003.
[30] Bunaziv I, Frostevarg J, Akselsen OM, Kaplan AFH. Process stability during fiber laser-arc hybrid welding of thick steel plates. Opt Lasers Eng 2018;102:34–44.
[31] Kluken AO, Grong ØJMTA. Mechanisms of inclusion formation in Al − Ti − Si − Mn deoxidized steel weld metals. Metall Trans A 1989;20:1335–49.
[32] Bunaziv I, Akselsen OM, Frostevarg J, Kaplan AFH. Deep penetration fiber laser-arc hybrid welding of thick HSLA steel. J Mater Process Technol 2018;256:216–28.
[33] Díaz-Fuentes M, Iza-Mendia A, Gutiérrez I. Analysis of different acicular ferrite microstructures in low-carbon steels by electron backscattered diffraction. Study of their toughness behavior. Metall Mater Trans A 2003;34:2505–16.
[34] Ricks RA, Howell PR, Barritte GS. The nature of acicular ferrite in HSLA steel weld metals. J Mater Sci 1982;17:732–40.
[35] Bunaziv I, Akselsen OM, Frostevarg J, Kaplan AFH. Laser-arc hybrid welding of thick HSLA steel. J Mater Process Technol 2018;259:75–87.
[36] Cho W-I, Na S-J, Cho M-H, Lee J-S. Numerical study of alloying element distribution in CO2 laser–GMA hybrid welding. Comput Mater Sci 2010;49:792–800.
[37] Wang H, Nakanishi M, Kawahito Y. Dynamic balance of heat and mass in high power density laser welding. Opt Express 2018;26:6392–9.
[38] Wu D, Hua X, Huang L, Li F, Cai Y. Observation of the keyhole behavior, spatter, and keyhole-induced bubble formation in laser welding of a steel/glass sandwich. Weld World 2019.
[39] Aucott L, Dong H, Mirihanage W, Atwood R, Kidess A, Gao S, et al. Revealing internal flow behaviour in arc welding and additive manufacturing of metals. Nat Commun 2018;9:5414.
[40] Hunter JD. Matplotlib: A 2D graphics environment. Comput Sci Eng 2007;9:90–5.